*Article*

# Catalytic Reduction of p-Nitrophenol on MnO₂/Zeolite -13X Prepared with *Lawsonia inermis* Extract as a Stabilizing and Capping Agent

**Enshirah Da'na** [1,*] **, Amel Taha** [2,3,*] **and Mohamed R. El-Aassar** [4]

1    Department of Biomedical Engineering, King Faisal University, P.O. Box 400, Alahsa 31982, Saudi Arabia
2    Department of Chemistry, King Faisal University, P.O. Box 400, Alahsa 31982, Saudi Arabia
3    Department of Chemistry, Faculty of Science and Technology, Al-Neelain University, Khartoum 1112, Sudan
4    Department of Chemistry, College of Science, Jouf University, Sakaka 2014, Saudi Arabia
*    Correspondence: edana@kfu.edu.sa (E.D.); ataha@kfu.edu.sa (A.T.);
     Tel.: +966-135897540 (E.D.); Fax: +966-135899557(E.D.)

**Abstract:** p-nitrophenol (pNP) is a highly toxic organic compound and is considered carcinogenic and mutagenic. It is a very stable compound with high resistance to chemical or biological degradation. As a result, the elimination of this pollutant has been very challenging for many researchers. Catalytic reduction is one of the most promising techniques, if a suitable catalyst is developed. Thus, this work aims to prepare an eco-friendly catalyst via a simple and low-cost route and apply it for the conversion of the toxic p-nitrophenol (pNP) into a non-toxic p-aminophenol (pAP) that is widely used in industry. Manganese oxide was prepared in an environmentally friendly manner with the aid of *Lawsonia inermis* (henna) extract as a stabilizing and capping agent and loaded on the surface of 13X molecular sieve zeolite. The UV-Vis spectrum, EDS, and XRD patterns confirmed the formation of the pure MnO₂ loaded on the zeolite crystalline network. The TGA analysis showed that the samples prepared by loading MnO₂ on zeolite (Mn2Z, Mn3Z, and Mn4Z) lost more mass than pure MnO₂ (Mn) or zeolite (Z), which is mainly moisture adsorbed on the surface. This indicates a better dispersion of MnO₂ on the surface of zeolite compared to pure MnO₂, and thus a higher number of active adsorption sites. SEM images and EDS confirmed the dispersion of the MnO₂ on the surface of the zeolite. Results showed a very fast reduction rate, following the order Mn2Z > Mn3Z > Mn4Z > Mn > Z. With sample Mn2Z, 96% reduction of pNP was achieved in 9 min and 100% in 30 min. For Mn3Z, Mn4Z, and Mn, 98% reduction was achieved in 20 min and 100% in 30 min. Zeolite was the slowest, with only a 40% reduction in 30 min. Increasing the amount of zeolite in the synthesis mixture resulted in lower reduction efficiency. The kinetic study indicated that the reduction of p-nitrophenol on the surface of the prepared nanocomposite follows the pseudo-first-order model. The results show that the proposed nanocomposite is very effective and very promising to be commercially applied in water treatment, due to its low cost, simple synthesis procedure, and reusability.

**Keywords:** zeolite; 13X molecular sieve; p-nitrophenol; p-aminophenol; catalytic reduction; manganese oxide; nanoparticles

## 1. Introduction

p-nitrophenol (pNP) is a highly toxic organic compound that is discharged to the water system from the pharmaceutical, photographic, fungicides, medicines, hair dyeing agents, leather, and corrosion inhibitors industries [1]. It causes many skin diseases and is considered carcinogenic and mutagenic [2]. Owing to the presence of the nitro group, pNP is a very stable compound with high resistance to chemical or biological oxidation [3]. Accordingly, many techniques such as adsorption [4], photocatalytic degradation [5], ozonation [6], membrane [7], microbial treatment [5], and electrocoagulation [8] have been applied for the removal of pNP from water. Among these processes, the conversion of the pNP into

p-aminophenol (pAP) is very promising, because of its high efficiency, low cost, and simple operation [9,10]. Furthermore, when pNP is reduced, it forms pAP, which is non-toxic and widely used in pharmaceuticals [11,12], dyes, polymers, papers, explosives, corrosion inhibitors, and anti-corrosion lubricant [12–14].

Although microbial treatment of pNP provides an effective and safe method compared to the chemical treatment methods, it shows major shortcomings related to slow reaction rate and difficulty in finding suitable microorganisms [5]. In addition, it is vital to consider the cost, the feasibility of scaling up the process, environmental regulations, and operation requirements such as safety, maintenance, control, and robustness. Despite the feasibility of sodium borohydride ($NaBH_4$) in reducing pNP, without a suitable catalyst, this reaction requires a high temperature and high hydrogen pressure [5]. Otherwise, this reduction is very slow [15]. Thus, it is crucial to find a suitable catalyst for this reaction to be able to take place under moderate conditions.

In the literature, a few researchers have reported the reduction of pNP over metal-free catalysts such as graphene and MOFs-based catalysts [12,16]. However, metal [17–22] and metal oxide [21–25] nanoparticles and nanocomposites have widely been applied, due to their excellent efficiency in lowering the reduction potential value [26–28]. Furthermore, their adaptable morphological, structural, chemical, physical, and optical properties have contributed to utilizing them in a wide area of research, including sensing, imaging, electronics, adsorption, and heterogeneous catalysis [15]. Additionally, the reduction of pNP using metal and metal oxide nanoparticle catalysts is very attractive, since it can be achieved in the aqueous solution [11]. Catalytic reduction of pNP to pAP with the aid of sodium borohydride ($NABH_4$) on a nanoparticles catalyst has been investigated extensively in the literature with different types of nanoparticles or nanocomposite, such as AuCu/Pt nano alloy [15], silver nanoparticles [29], Au-$ZrO_2$ nanocatalyst [30], Au [31], Pt, and Pd/SBA-15 [3], FeNi [27], $Co_9S_8$ [26], Pd/$TiO_2$, [23], CuO, [24], magnetic Pt nanocomposites [32], Au-Pd [9], Au [33], $SrTiO_3$/Ag [34], $MoS_2$/ZnO [35], Ag/graphene [13], Au/$TiO_2$ [25], PtPdBi, [36], Ag/ZnO/AC [37], Au/AC [2], Fe/chitosan [11], and Pd [17].

The catalytic performance of metals/oxide is strongly related to the particle size distribution and the dispersion of the nanoparticles on the surface of the support, if any exist [3]. Accordingly, one major requirement for a good nanoparticles-based catalyst is to minimize aggregation. Much effort has been dedicated to preparing hybrid catalysts by immobilizing nanoparticles on a surface of suitable support, such as activated carbon [2], silica-based materials [38], metal, chitosan [11], graphene [39], polymers [28], and zeolite [40]. Among all the reported supports, zeolites are considered very attractive supports for nanoparticles due to their high thermal stability, high surface area, nanoporous crystalline structure, stability in organic solvents, non-toxicity, eco-friendliness, availability at low cost, and corrosion resistance [40]. Accordingly, they have been used to support a wide range of nanoparticles for different applications [40–44].

The other strategy for minimizing aggregation is to surround the nanoparticles with a layer to protect aggregation. This layer could be polymeric materials, organic functionality, or a surfactant. Recently, a new approach was developed by utilizing plant extract as a stabilizing and capping agent [37,45–51]. The synthesis of nanoparticles with the aid of plant extracts offers a cheaper, safer, and eco-friendly pathway, since it removes the need for extra chemicals as reduction and capping agents. In addition, these plants are usually plentifully available at no or very low cost [31].

*Lawsonia inermis* (henna) belongs to the family Lythraceae and is a flowering plant, 2–6 m in height. *L. inermis* grows in North Africa, Asia, America, Australia, Egypt, and India [52]. The important natural constituents of *L. inermis* include tannins, phenolic compounds, alkaloids, and flavonoids, which are considered very effective reduction and capping agents [53].

MnO$_2$ nanoparticles have been applied widely in catalysis, adsorption, oxidation reactions, dry cells, pigment, ceramics, electrodes, and batteries [43]. However, MnO$_2$ has a major drawback related to its irregular pore structure that decreases the available surface area and, accordingly, the catalytic efficiency [40]. Furthermore, fine particles formed at relatively low temperatures tend to aggregate at high temperatures, leading to coarse crystalline materials with a particle size in the range of 2.5–10 μm. Similarly, the surface area decreases with an increase in the particle size distribution [54]. A promising solution for this shortcoming is to combine MnO$_2$ with suitable support. In this regard, so far, a few studies have reported the synthesis of MnO$_2$/zeolite composite. Thus, in this work, an effective and eco-friendly catalyst will be prepared by combining 13X zeolite molecular sieve as support with MnO$_2$ nanoparticles prepared with the aid of *L. inermis* extract as a stabilizing and capping agent. The attractive characteristics of the proposed catalyst include the very simple and low-cost synthesis procedure, which eliminates the need for harsh chemicals such as NABH$_4$ or critical conditions such as high temperature, the flow of inert gas, or multiple steps.

## 2. Materials

*Lawsonia inermis* (henna) powder was purchased from the local market of Al-Ahsa, Saudi Arabia. Zeolite (13X molecular sieves) (composition Na$_2$O$_3$, SiO$_2$, H$_2$O) was purchased from ThermoFisher, Waltham, MA, USA. MnCl$_2$·4H$_2$O (purity $\geq$ 99%), NaOH (purity $\geq$ 98%), and p-Nitrophenol (purity $\geq$ 99%) were supplied by Sigma-Aldrich (St. Louis, MO, USA) and used as received.

## 3. Method

### 3.1. Preparing Lawsonia inermis (Henna) Extract

To prepare the Henna extract (HE), 10 g of the plant root powder was mixed with 100 mL of distilled water. The mixture was boiled for 10 min then left overnight. After that, the mixture was filtered with Whatman filter paper and the filtrate was kept in the fridge until it was used.

### 3.2. Preparing the MnO$_2$ Nanoparticles (M)

Henna extract (25mL) was mixed with 100 mL of 0.1 M MnCl$_2$·4H$_2$O solution. The pH of the mixture was adjusted to 11 using 1 M NaOH and an Orion 2-Star pH meter. The mixture was then stirred at room temperature and 70 rpm for 24 h. After that, the mixture was filtered and the solid was washed with distilled water and then ethanol. Finally, it was dried in a convection oven at 100 °C for 3 h, then collected and kept in a sealed container until it was used.

### 3.3. Preparing the MnO$_2$ Nanoparticles Loaded on Zeolite

Figure 1 shows the steps followed in the synthesis of MnO$_2$/Zeolite. Specifically, 100 mL of 0.1 M MnCl$_2$·4H$_2$O solution was mixed with 25 mL of the henna extract. A certain mass of zeolite (13X molecular sieves), according to Table 1, was added to the mixture and it was stirred for 30 min. The pH of the mixture was adjusted to 11 using 1 M NaOH and an Orion 2-Star pH meter. The mixture was then stirred at room temperature and 70 rpm for 24 h. After that, the mixture was filtered and the solid was washed with distilled water and then ethanol. Finally, it was dried in a convection oven at 100 °C for 3 h, then collected and kept in a sealed container until it was used.
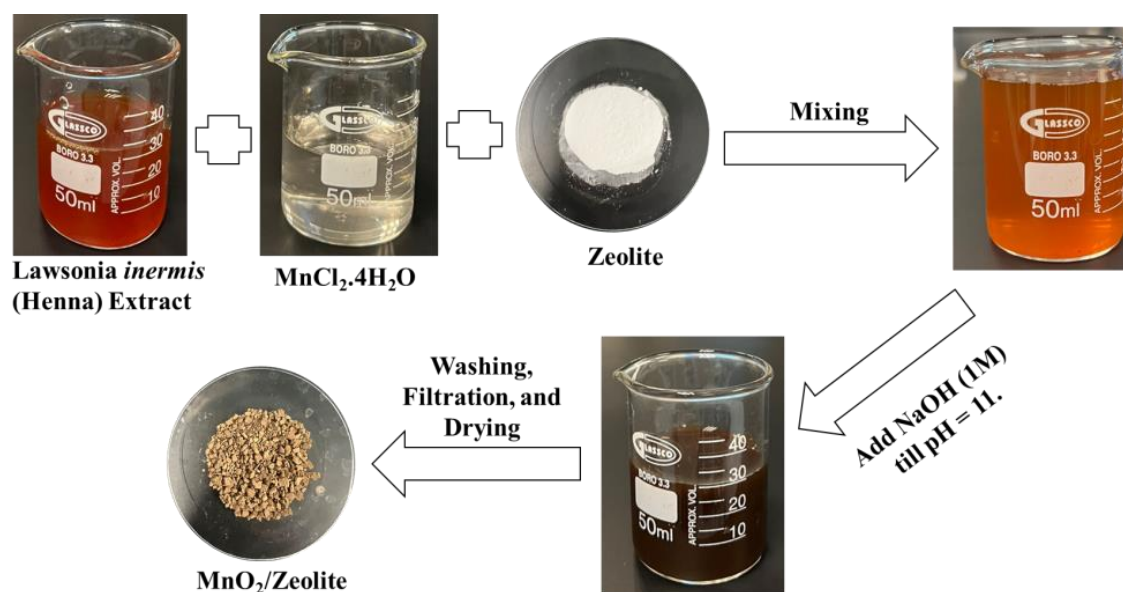
**Figure 1.** Schematic diagram of the synthesis of $MnO_2$/Zeolite nanocomposite.

**Table 1.** Details of $MnO_2$/Zeolite nanocomposite and $N_2$ adsorption results.

| Sample | Amount of Zeolite (g) | BET Surface Area ($m^2g^{-1}$) | PJH Pore Volume ($cm^3g^{-1}$) | PJH Pore Diameter (nm) |
|---|---|---|---|---|
| Mn | 0 | 4.45 | 0.0092 | 3.17 |
| Mn2Z | 2 | 32.22 | 0.097 | 1.77 |
| Mn3Z | 3 | 29.45 | 0.131 | 1.56 |
| Mn4Z | 4 | 22.78 | 0.058 | 1.76 |
| Z | Pure zeolite | 406.75 | 0.722 | 1.89 |

## 4. Characterization

To confirm the formation of $MnO_2$, all the nanocomposite samples were analyzed by X-ray diffraction (XRD) using XRD-7000 with a Cu-detector (Shimadzu, Tokyo, Japan) over the 2θ range of 10–80°. Furthermore, they were dispersed in distilled water and the UV-Vis spectra were recorded for the wavelength range of 200–1100 nm using a UV-Vis spectrophotometer (Shimadzu, Tokyo, Japan). To test the thermal stability of the prepared samples, thermal gravimetric analysis (TGA) was conducted under nitrogen with a temperature ramp of 2°/min from 20 °C to 500 °C using a TGA-51 Shimadzu Thermogravimetric Analyzer (Tokyo, Japan). Dynamic light scattering (DLS) analysis was performed for the $MnO_2$ nanoparticles to calculate the particle size distribution. This analysis was performed with a Thermo Scientific, Quattro S, USA. Scanning electron microgram (SEM) imaging was performed for all samples using a Thermo Scientific, Quattro S, USA. FTIR analysis was performed with a Thermo Scientific, Quattro S, USA for the wavenumber range of 4000–4000 $cm^{-1}$. Nitrogen adsorption was measured for all samples after degassing the samples at 70 K, and the BET technique was performed to estimate the surface area. This analysis was performed with a NOVA 4200e (Quantachrome Instruments, B Beach, FL, USA).

### 4.1. Catalytic Reduction of p-Nitrophenol (pNP)

To study the catalytic activity of the prepared samples, 3 mL of 20 $mgL^{-1}$ pNP solution was mixed with 1 mg of $NaBH_4$ and 10 mg of Z, Mn2Z, Mn3Z, Mn4Z, or Mn was added to the solution; the concentration of pNP was monitored as a function of time by measuring the UV absorbance at 400 nm every 3 min for 30 min, using a UV-Vis spectropho-

tometer (Shimadzu, Tokyo, Japan). The removal percentage of pNP was calculated with Equation (1):

$$R\% = \frac{A_0 - A_t}{A_0} \times 100\% \tag{1}$$

where $A_t$ and $A_0$ are the absorbance of p- nitrophenolate ion at any time t and at time zero, respectively. The kinetics of the catalytic reduction were tested with pseudo-first-order kinetics. The linear form of this kinetic model is given in Equation (2). The rate constants (k), were evaluated by plotting Ln ($A_t$) versus time. The slope value of the straight line represents the rate constant k (min$^{-1}$).

$$Ln\,(A_t) = Ln\,(A_0) - kt \tag{2}$$

For the recycling experiment, the catalyst was collected by filtration, washed thoroughly with deionized water, and reused in the catalytic cycles.

*4.2. FTIR Analysis*

Figure 2 shows the FTIR spectra for Z, Mn2Z, Mn3Z, Mn4Z, Mn, and the plant extract (HE). All the patterns have a broad peak in the wavenumber range of ~3200–3600 cm$^{-1}$, which is assigned to stretching vibrations of the O–H in hydrogen-bonded internal silanol groups and O–H stretching of water attached to the surface [41] The peak at ~1620 cm$^{-1}$ is related to vibration bending of coordinated (–OH) groups attached to the zeolite surface. The peak at ~450 cm$^{-1}$ in Mn2Z, Mn3Z, Mn4Z, and Mn is assigned to the Mn-O bond [14,42], while the peak at ~450 cm$^{-1}$ in Z is related to the bending vibrations of Si–O and Al–O in zeolites [40]. The peak at ~740 cm$^{-1}$ in Mn2Z, Mn3Z, Mn4Z, and Z is assigned to the stretching vibration of Al–O [55], while the peak at ~960 cm$^{-1}$ in the same samples is related to Si–O stretching vibrations, and the asymmetric stretching of Si–O–Al tetrahedral [55]. In the HE pattern, the peak at ~1437 cm$^{-1}$ is assigned to the C-O bond and that at ~1668–1725 cm$^{-1}$ is related to the stretching vibration of the C=O cm$^{-1}$ group of the effective compounds in the extract.
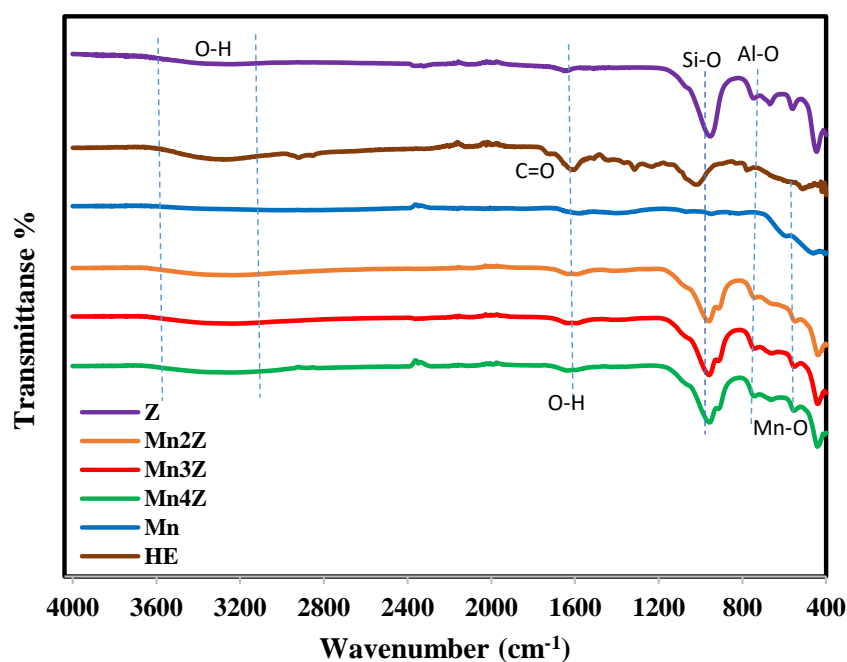


**Figure 2.** FTIR spectrum of, Z, Mn2Z, Mn3Z, Mn4Z, Mn, and HE for the wavenumber range 4000–400 cm$^{-1}$. Spectra were shifted vertically for better visibility.

### 4.3. UV Analysis

Figure 3 shows the UV-Vis spectra of Mn2Z, Mn3Z, Mn4Z, and Mn for the wavelength range of 200–1100 nm. The presence of the absorbance band in the range of 240–300 nm confirms the successful production of MnO nanoparticles. The shift of the absorption bands shows that different morphologies and sizes are presented [56].
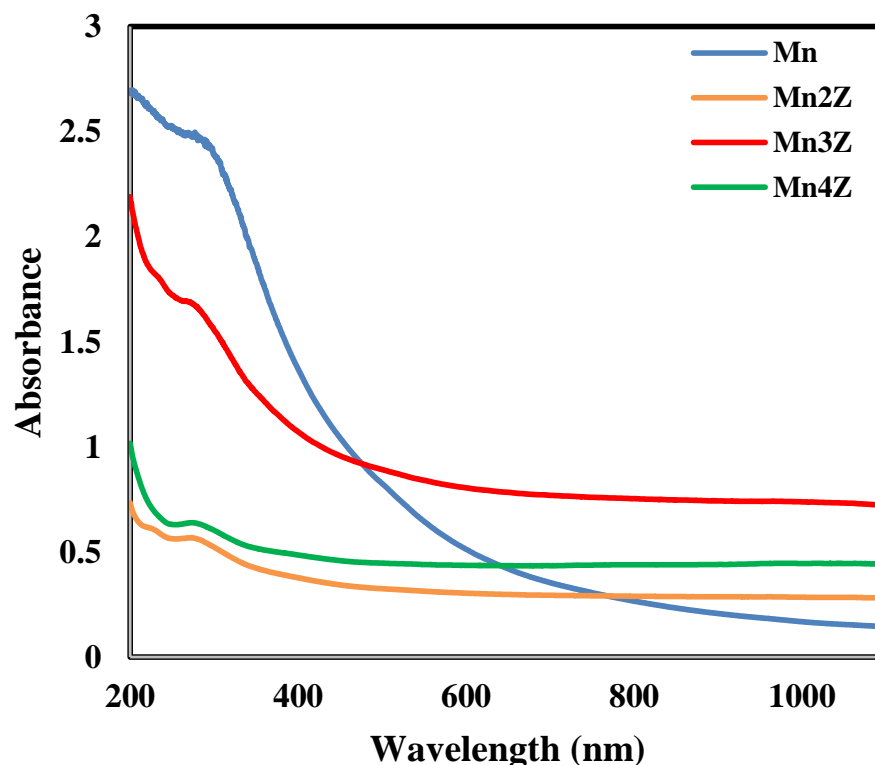


**Figure 3.** The UV-Vis spectra of Mn2Z, Mn3Z, Mn4Z, and Mn for the wavelength range of 200–1100 nm.

### 4.4. TGA Analysis

The TGA profile of the five samples is shown in Figure 4 for the temperature range of 20–500 °C. Pure $MnO_2$ has the highest stability, with a mass loss of only 10%, which is mainly related to the water adsorbed on the surface. Bare zeolite lost 22%, mainly in the temperature range of 150–250 °C, which is also attributed to the water adsorbed on the surface. The three samples prepared by loading $MnO_2$ on the surface of zeolite showed a higher mass loss (24–26%) within the same temperature range, indicating that the nanocomposite samples have higher adsorption capacity toward moisture. This indicates a better dispersion of $MnO_2$ on the surface of zeolite compared to pure $MnO_2$, and thus a higher number of active adsorption sites.

### 4.5. XRD Analysis

The phase purity and crystallinity of the prepared samples were investigated by X-ray diffraction technique (XRD), and the results are shown in Figure 5. The XRD patterns of Mn, Mn2Z, Mn3Z, and Mn4Z show peaks at 2θ values of 19.2, 28.6, 40.8, 50.4, and 66.6, which are attributed to (200), (310), (301), (411), and (002) crystal planes, respectively [57]. The presence of these diffraction peaks confirms the presence of the α-$MnO_2$ crystal phase, according to the standard data (JCPDS card number 44-0141) [58]. Furthermore, extra peaks appear in the pattern of Mn2Z, Mn3Z, and Mn4Z at 2θ of 11.73, 15.2, 20.1, 23.3, 26.7, 31, and 33.8, corresponding to the planes of (311), (331), (440), (533), (642), (662), and (322), respectively, of the zeolite-13X substrate, which matches well with the pattern

shown in sample Z related to pure zeolite [42,57]. These results confirmed the successful impregnation of $MnO_2$ on the surface of zeolite-13X.
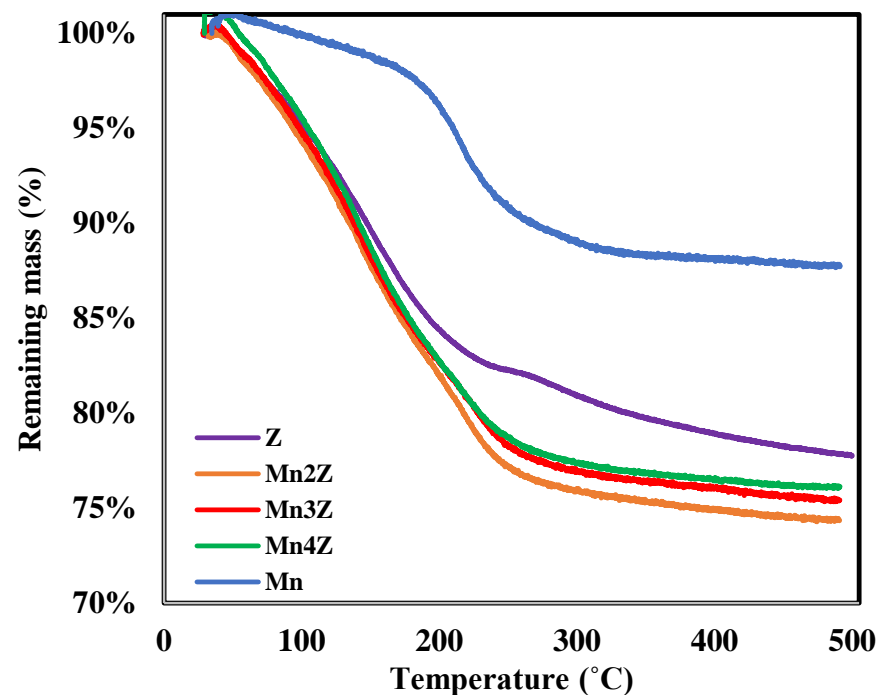


**Figure 4.** The TGA profile of, Z, Mn2Z, Mn3Z, Mn4Z, and Mn for the temperature range of 20–500 °C under nitrogen.
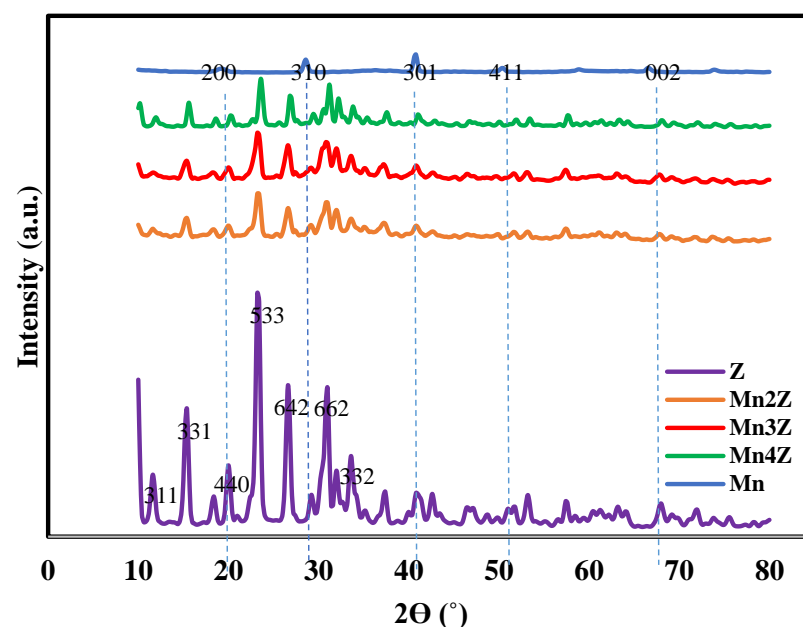


**Figure 5.** XRD patterns of, Z, Mn2Z, Mn3Z, Mn4Z, and Mn for the 2θ range 10–80°. Spectra were shifted vertically for better visibility.

*4.6. SEM and EDS Analysis*

The scanning electron micrograms of Mn, Mn2Z, Mn3Z, Mn4Z, and Z were taken at 5000× and 20,000× magnifications, as shown in Figure 6. The SEM data of bare zeolite show the typical crystalline structure, with smooth edges and crystallite sizes in the range

of ~5–10 μm. [59] After depositing the $MnO_2$ on the surface, the sharp edges are less clear for all samples. The images also indicate a good distribution of $MnO_2$ on the surface of the zeolite-13X support and a low degree of $MnO_2$ particle aggregation, with an average particle size of ~0.5 μm. Table 1 shows that the specific surface area, specific pore volume, and average pore diameter of pure zeolite, respectively, are 406.75 $m^2g^{-1}$, 0.722 $cm^3g^{-1}$, and 1.89 nm, indicating a microporous structure [60], while for the pure $MnO_2$, the values are, respectively, 4.45 $m^2g^{-1}$, 0.0092 $cm^3g^{-1}$, and 3.17 nm. The EDS shown in Figure 7 confirms the dispersion of $MnO_2$ on the surface of the zeolite. It is shown that the content of Mn decreased by increasing the ratio of zeolite in the sample, with Mn content of 56.3%, 12.8%, 10.1%, 9.9%, and 0.0% for Mn, Mn2Z, Mn3Z, Mn4Z, and Z, respectively.
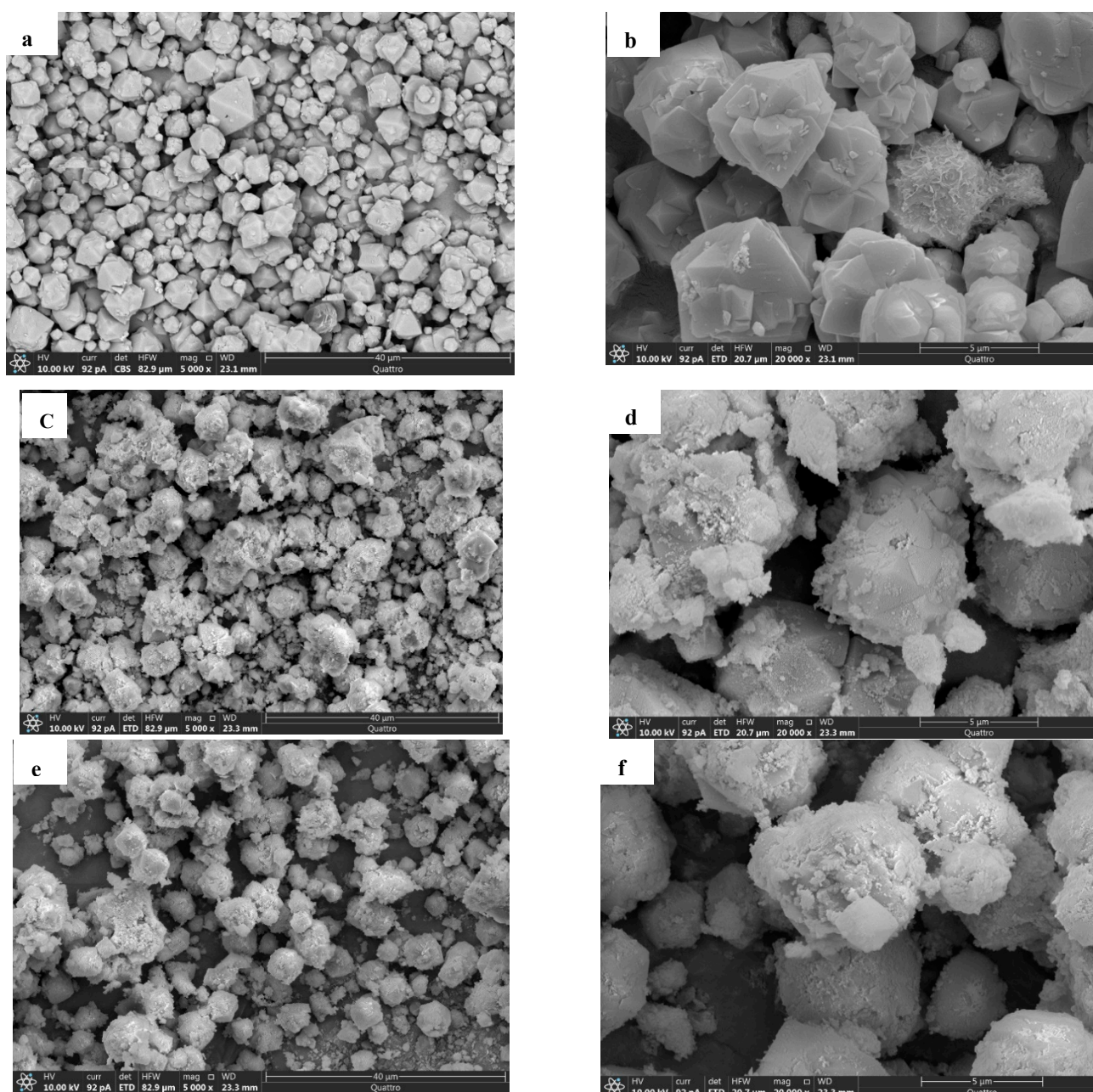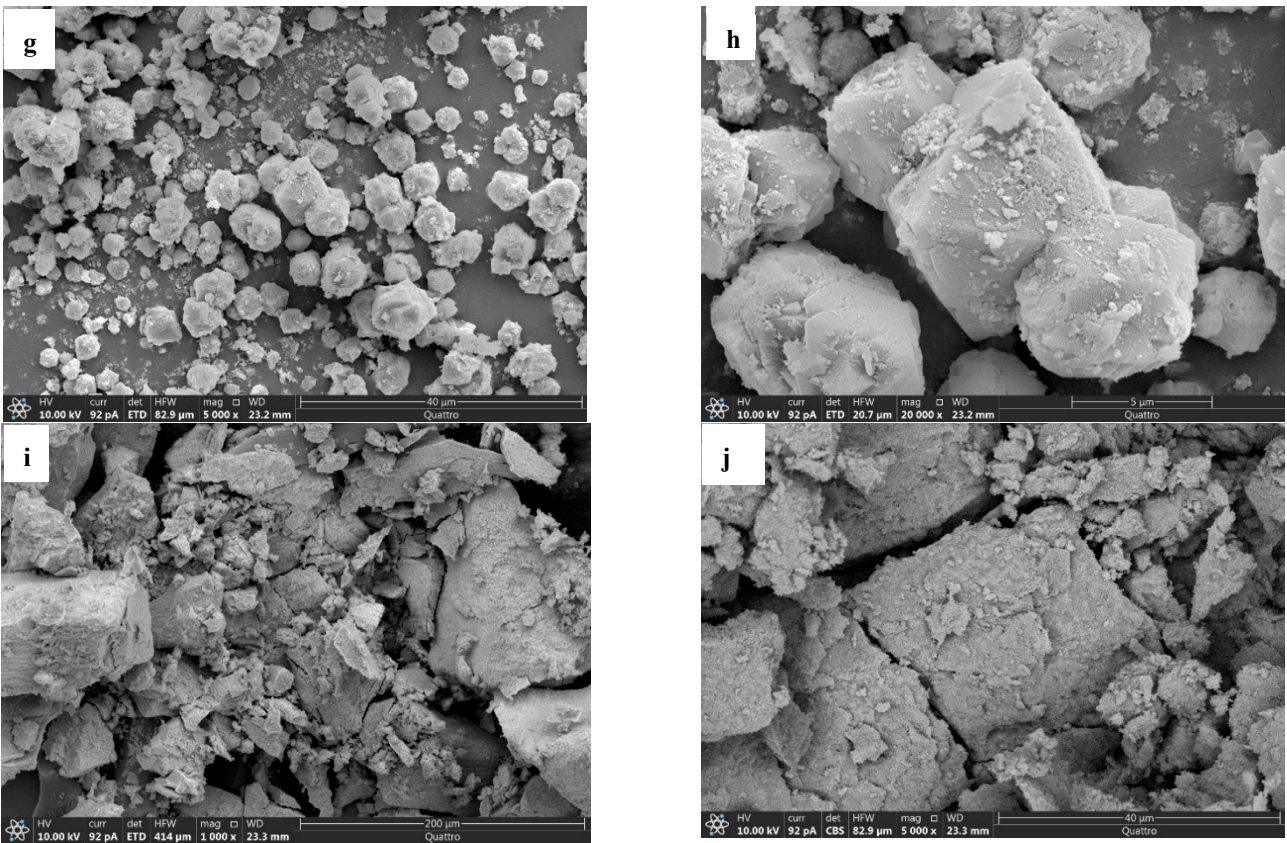


**Figure 6.** *Cont.*

**Figure 6.** SEM images for Z (**a**,**b**), Mn2Z (**c**,**d**), Mn3Z (**e**,**f**), Mn4Z (**g**,**h**), and Mn (**i**,**j**) at two different magnifications.



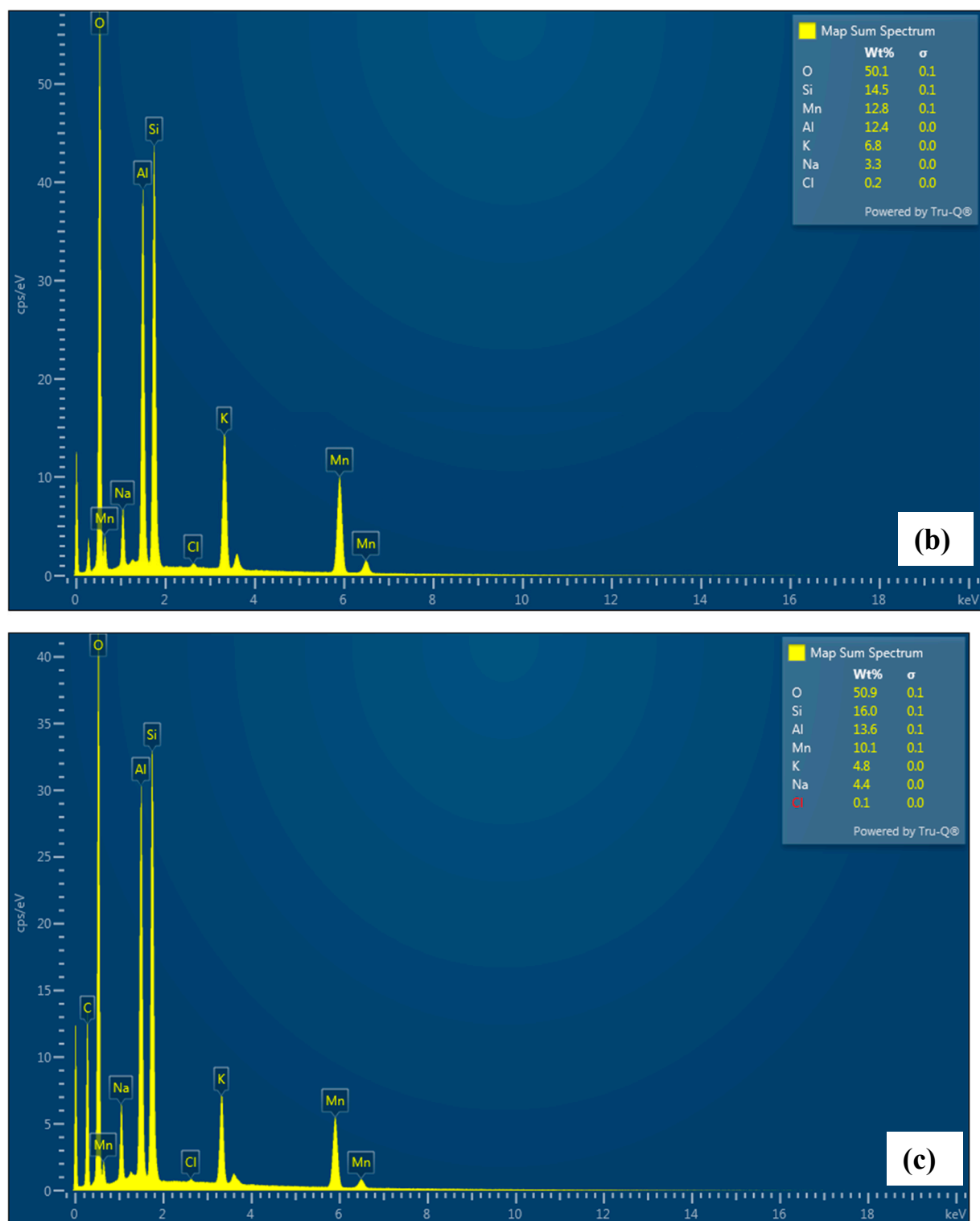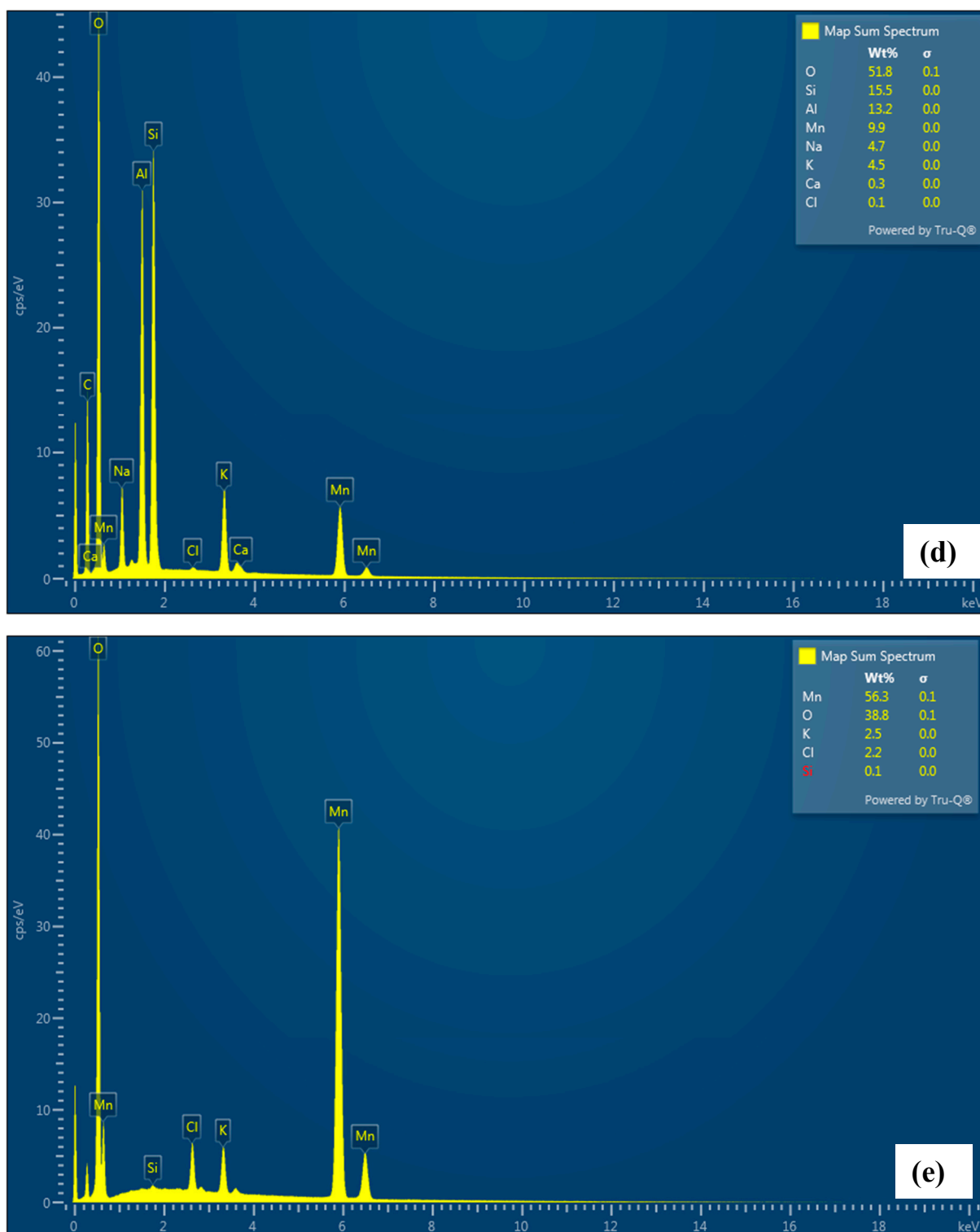**Figure 7.** *Cont*.

**Figure 7.** *Cont.*

**Figure 7.** EDS analysis for Z (**a**), Mn2Z (**b**), Mn3Z (**c**), Mn4Z (**d**), and Mn (**e**).

The nitrogen adsorption/desorption isotherms are shown in Figure 8a. According to the IUPAC classification, the pure zeolite exhibits type II adsorption isotherm with a very slow increase in the adsorbed volume until a $P/P_0$ of 0.8 is reached [60]. At this point, a sudden increase occurred due to the mesoporous structure of the zeolite sample. Furthermore, the appearance of the adsorption/desorption hysteresis loop is due to capillary condensation within the mesoporous structure. The isotherms for the samples

Mn2Z, Mn3Z, and Mn4Z exhibit the same pattern, with a drastic decrease in the volume adsorbed, as shown in Table 1. This is mainly related to the blockage of the pores of zeolite by the accumulation of $MnO_2$ particles. The isotherm of pure $MnO_2$ displays a non-porous nature, with a very low pore volume, as shown in Table 1. Thus, the combination of $MnO_2$ with the zeolite resulted in better dispersion of the nanoparticles, leading to a better catalytic activity, as will be discussed next. Combining $MnO_2$ with the zeolite resulted in a drastic decrease in the surface area, pore volume, and average pore diameter for Mn2Z, Mn3Z, and Mn4Z. This is mainly due to the blocking of the pores of zeolite (1.89 nm) with the $MnO_2$ particles, which have an average particle size distribution of around 600 nm, as shown in Figure 8b.
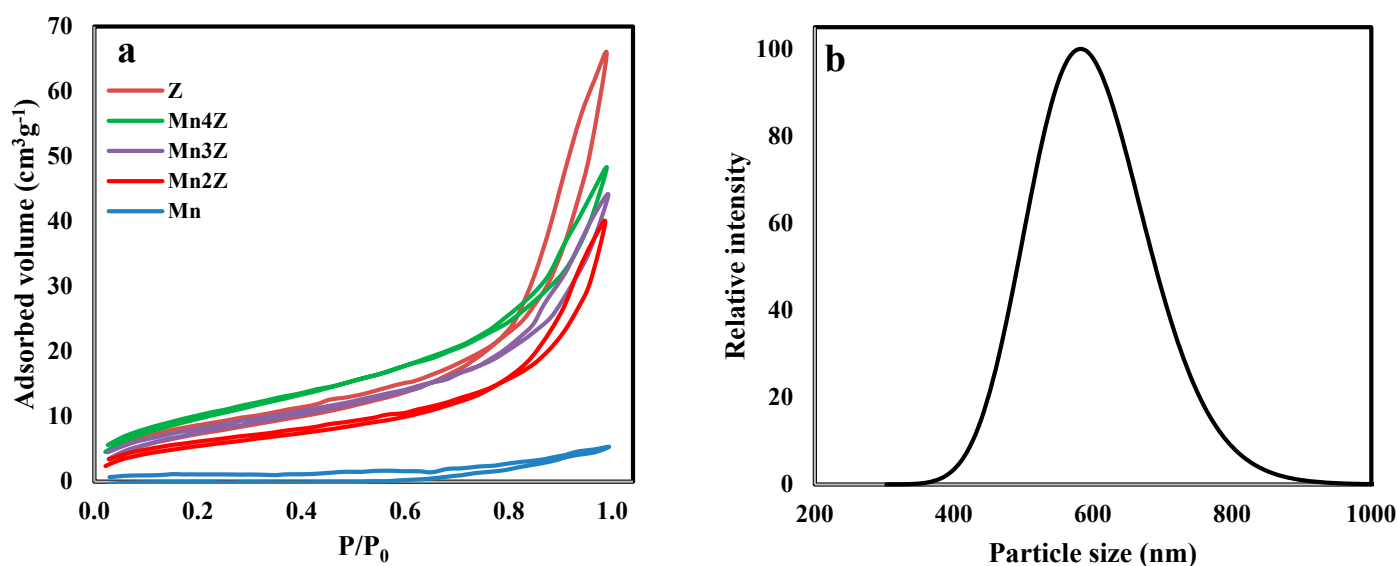


**Figure 8.** Nitrogen adsorption isotherms of Z, Mn2Z, Mn3Z, Mn4Z, and Mn (**a**), and DLS analysis of $MnO_2$ (**b**).

*4.7. Catalytic Reduction of p-Nitrophenol (pNP)*

The catalytic performance of the prepared nanocomposites was investigated using the reduction of p-nitrophenol into p-aminophenol according to the proposed mechanism shown in Figure 9. The characteristic absorption peak of pNP, which has a light yellow color as shown in Figure 10a, is located around 317 nm (Figure 11a). When $NaBH_4$ is added to pNP, without a catalyst, the solution color changed to dark yellow immediately (Figure 10b). Furthermore, the peak position shifted from 317 to 400 nm (Figure 11a). These changes are related to the formation of 4-nitrophenolate anions, according to Equation (3) [5,61]. When the catalyst was added to the solution in the presence of $NaBH_4$, the peak at 400 nm started to decrease, while a new peak around 300 nm started to appear and increase with time, due to the formation of pAP (Figure 11d–h). [2,5] Furthermore, the color of the solution started to disappear and it became colorless at the end of the reaction, as shown in Figure 10d–h, with the very large amount of gas bubbles confirming the reaction was taking place.
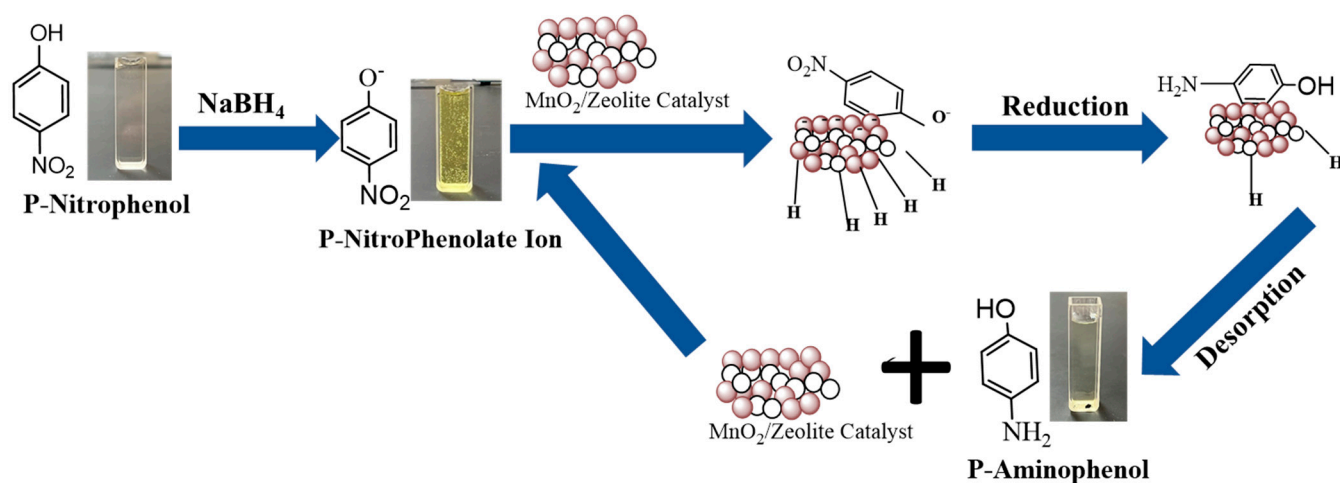
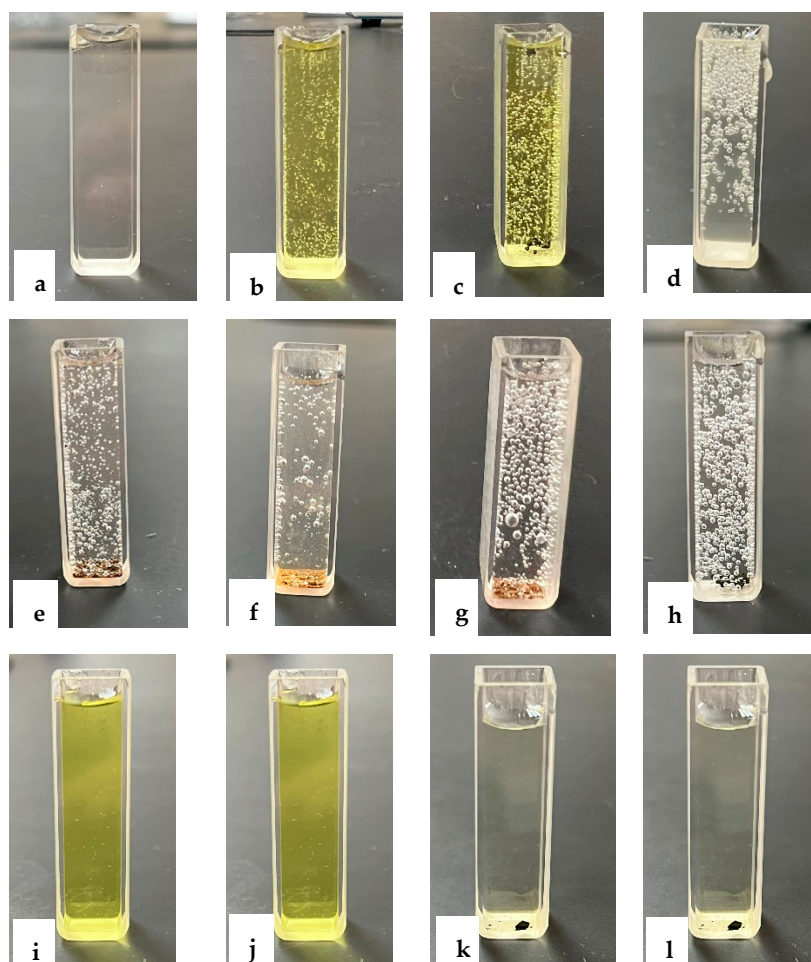**Figure 9.** The mechanism of catalytic conversion of pNP into pAP.



**Figure 10.** p-nitrophenol solution (20 mgL$^{-1}$) (**a**), p-nitrophenol solution (20 mgL$^{-1}$) directly after adding NaBH$_4$ (**b**), p-nitrophenol solution (20 mgL$^{-1}$) directly after adding NaBH$_4$ and catalyst (**c**), p-nitrophenol solution (20 mgL$^{-1}$) 30 min after adding NaBH$_4$ and Z (**d**), Mn2Z (**e**), Mn3Z (**f**), Mn4Z (**g**), Mn(**h**), and without adding catalyst (**i**). p-nitrophenol solution (20 mgL$^{-1}$) 30 min and 24 h after adding NaBH$_4$ (**i**,**j**). p-nitrophenol solution (20 mgL$^{-1}$) 30 min and 24 h after adding Mn2Z without NaBH$_4$ (**k**,**l**).
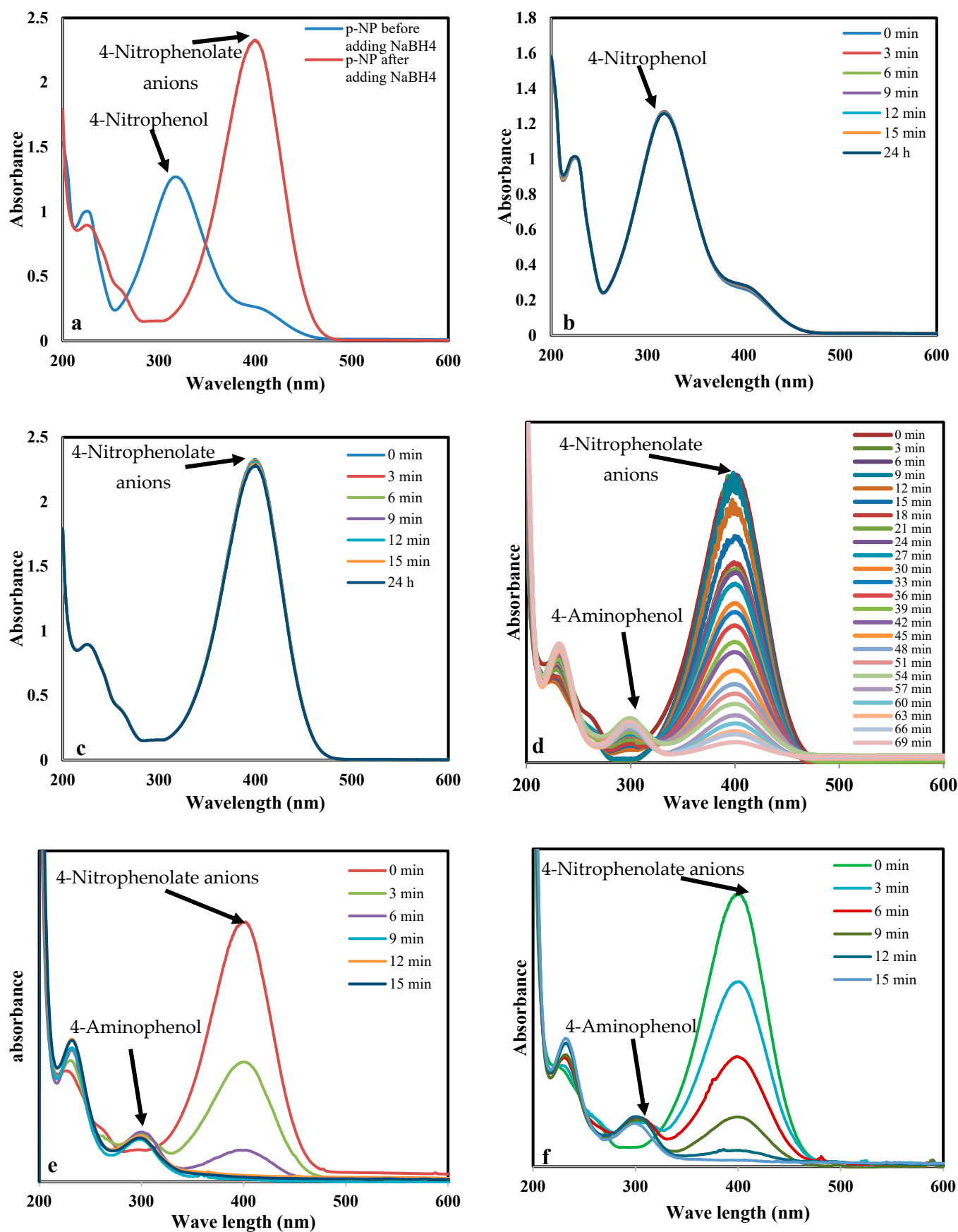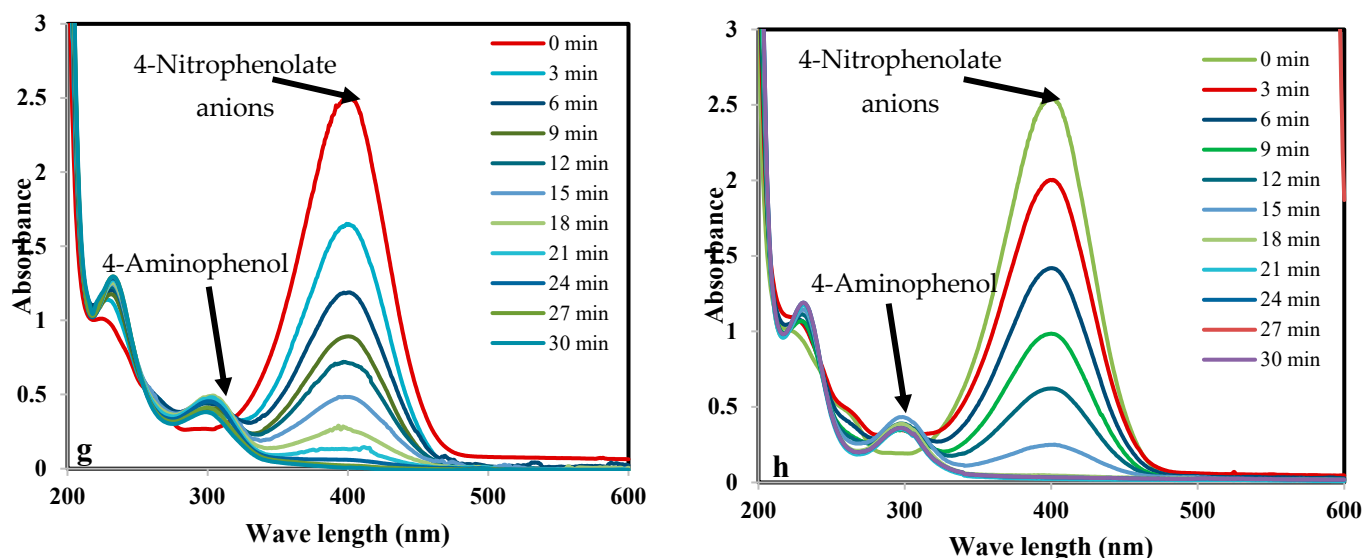
**Figure 11.** *Cont.*

**Figure 11.** Time-dependent UV-Vis spectral changes of the pNP solution catalyzed by Z, Mn2Z, Mn3Z, Mn4Z, and Mn. The reduction conditions were: 3mL of 20 mgL$^{-1}$ pNP solution, 1 mg NaBH$_4$, and 10 mg of the catalyst.

Two blank tests were performed to confirm the necessity of both catalyst and NaBH$_4$. In the absence of NaBH$_4$, adding the catalyst to the p-nitrophenol solution did not result in any reduction after 24 h (Figures 10k, 8i and 10b). This is mainly because the formation of p-nitrophenolate requires high pressure of hydrogen that is achieved by adding NaBH$_4$ [5]. Furthermore, adding NaBH$_4$ without the nanocomposites did not initiate the reduction into p-aminophenol, as observed from the solution color, which did not change after 24 h, as shown in Figure 10i,j. Furthermore, in the presence of nanocomposites without adding NaBH$_4$ to the reaction mixture, there was no reduction or change in the absorbance peak (Figure 11c). Thus, for reduction to occur, both NaBH$_4$ and nanocomposite are needed.

Figure 11 shows the time-dependent UV-Vis absorption spectra for the reduction of pNP with the aid of Z, Mn2Z, Mn3Z, Mn4Z, and Mn. The difference between Z, Mn2Z, Mn3Z, Mn4Z, and Mn is the catalytic activity and, thus, the time required to reach 100% reduction of pNP and the disappearance of the absorption peak at 400 nm. This peak decreased very slowly in sample Z, while Mn2Z showed the fastest rate of reduction. The high efficiency of Mn2Z may be related to the ratio of MnO$_2$, which resulted in good loading of MnO$_2$, with good distribution on the surface, leading to efficient accessibility of the reactants to the active sites and high catalytic performance.

Figure 12a shows the reduction percentage of pNP as a function of time for the five samples. It shows that Mn2Z is very fast, with a 96% reduction achieved in 9 min, compared to 82%, 65%, 61%, and 3% achieved by Mn3Z, Mn4Z, Mn, and Z, respectively. A complete reduction was observed by 30 min for all samples except the bare zeolite, with only a 40% reduction achieved. The performance of the nanocomposites prepared by combining the zeolite as support with the MnO$_2$ (Mn2Z, Mn3Z, and Mn4Z) showed higher activity than Z and Mn. This is mainly related to improving the dispersion of MnO$_2$ and thus minimizing the aggregation, resulting in a higher surface area and a higher number of active sites available for the reduction process. A pseudo-first-order kinetic model was used to fit the data, as shown in Figure 12b and Table 2. The results show that all the samples fit well with the pseudo-first-order kinetic model, with an R$^2$ value of more than 0.90. The k values support the activity order of Mn2Z > Mn3Z > Mn $\cong$ Mn4Z >> Z.
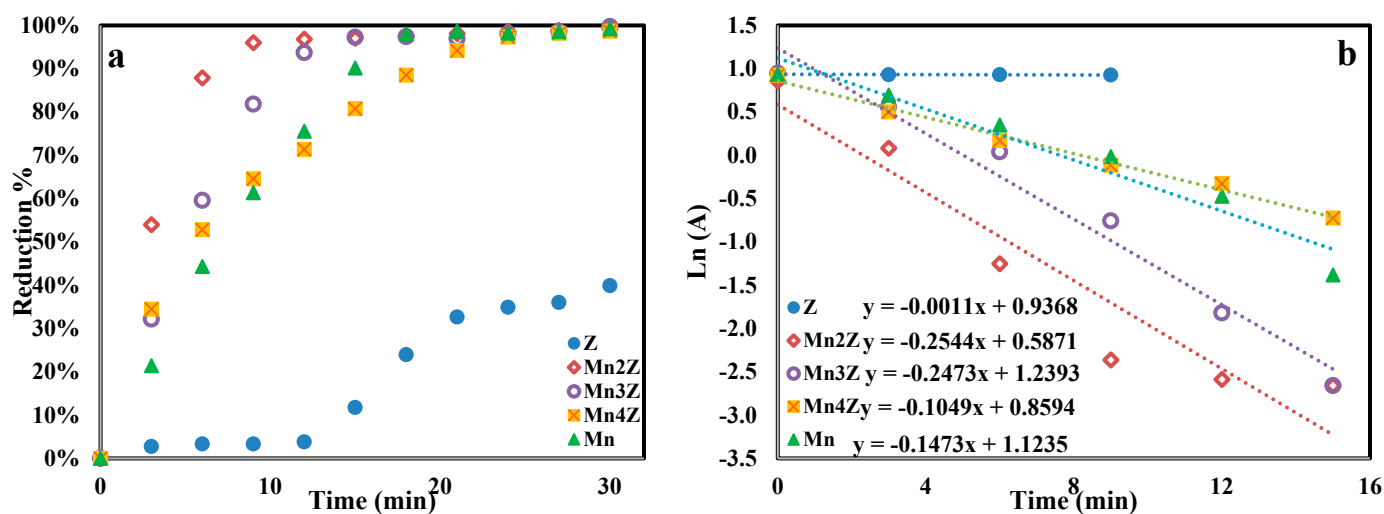
**Figure 12.** The efficiency of the catalytic reduction of pNP over Z, Mn2Z, Mn3Z, Mn4Z, and Mn nanocomposites (**a**), The linear plot of the pseudo-first-order kinetics reduction of pNP over Z, Mn2Z, Mn3Z, Mn4Z, and Mn nanocomposites (**b**). The reduction conditions were: 3 mL of 20 mgL$^{-1}$ pNP solution, 1 mg NaBH$_4$, and 10 mg of the catalyst.

**Table 2.** The fitting parameters of the linear plot of the pseudo-first-order kinetics reduction of pNP over Z, Mn2Z, Mn3Z, Mn4Z, and Mn nanocomposites.

|  | **Z** | **Mn2Z** | **Mn3Z** | **Mn4Z** | **Mn** |
|---|---|---|---|---|---|
| k (min$^{-1}$) | 0.0011 | 0.2544 | 0.2473 | 0.1049 | 0.1473 |
| R$^2$ | 0.9000 | 0.9094 | 0.9730 | 0.9912 | 0.9447 |

Table 3 shows a comparison of the reduction percentage obtained in this work with some other catalysts reported in the literature. As can be seen, the time required to complete the reduction in this study is comparable to most of the previously reported results. However, the catalyst reported in this work can be prepared from low-cost precursors and via very simple procedures, without the need for complicated conditions such as high temperature, multiple steps, a flow of inert gas, or the use of harmful chemicals such as NaBH$_4$ or KBH$_4$, as shown in Table 3. Furthermore, the developed catalyst showed very good reusability, by maintaining almost 95% of the original activity after four successive cycles, as shown in Figure 13.

**Table 3.** Catalysts reported in the literature for the reduction of p-nitrophenol.

| Catalyst | Operating Conditions | Degradation Efficiency | Ref. | Drawback |
|---|---|---|---|---|
| Ag/poly(norepinephrine)/ MnO$_2$ | 30 mL of 1 mM of 4-NP, 3 mL of 0.2 M of NaBH$_4$, and After that, 1 mg of catalyst. |  | [62] | Multiple-step synthesis |
| AuNPs | 2.5 mL of the 4-nitrophenol ($8 \times 10^{-5}$ M), 0.5 mL NaBH$_4$ (0.6 M), and 0.25 mL gold nanocatalyst. | 100% in 9 min. | [31] | Expensive precursors. |
| CuNPs | 1.7 mL of p-nitrophenol (0.1 mM), 0.7 mL of NaBH$_4$ (0.04 M), and an aqueous solution of Cu NCs (0.1 mL, 15 mM). | 100% in 10 min. | [63] |  |
| AuCu@Pt nanoalloys | 100 mL of 10 nM AuNPs,100 mL of 1 mM 4-NP, 3.5 mL NaBH$_4$ (100 mM). | 100% in 10 min. | [15] | Complicated synthesis, expensive precursors. |
| AuNPs | 2 mL of NaBH$_4$ (0.1 M), 1 mL of 4-nitrophenol ($2.0 \times 10^{-4}$ M), and 2 μL of AuNP. | 100% in 8 min. | [64] | Complicated synthesis, expensive precursors. |
| PtPdBi nanowire | 3.3 mL of 0.09 mM p-nitrophenol and 0.10 mL of 0.10 M NaBH$_4$ and 15 mg of the metal catalyst. | 100% in 24 min. | [36] | High temperature, flow of argon. |
| AgNPs | 4-NP (2 mL, $10^{-4}$ M), NaBH$_4$ (1 mL, $10^{-4}$ M), and AgNPs (2.5 μL, 6 nmol). | 96% in 3 min. | [20] | Use of NaBH$_4$ during synthesis. |

**Table 3.** *Cont.*

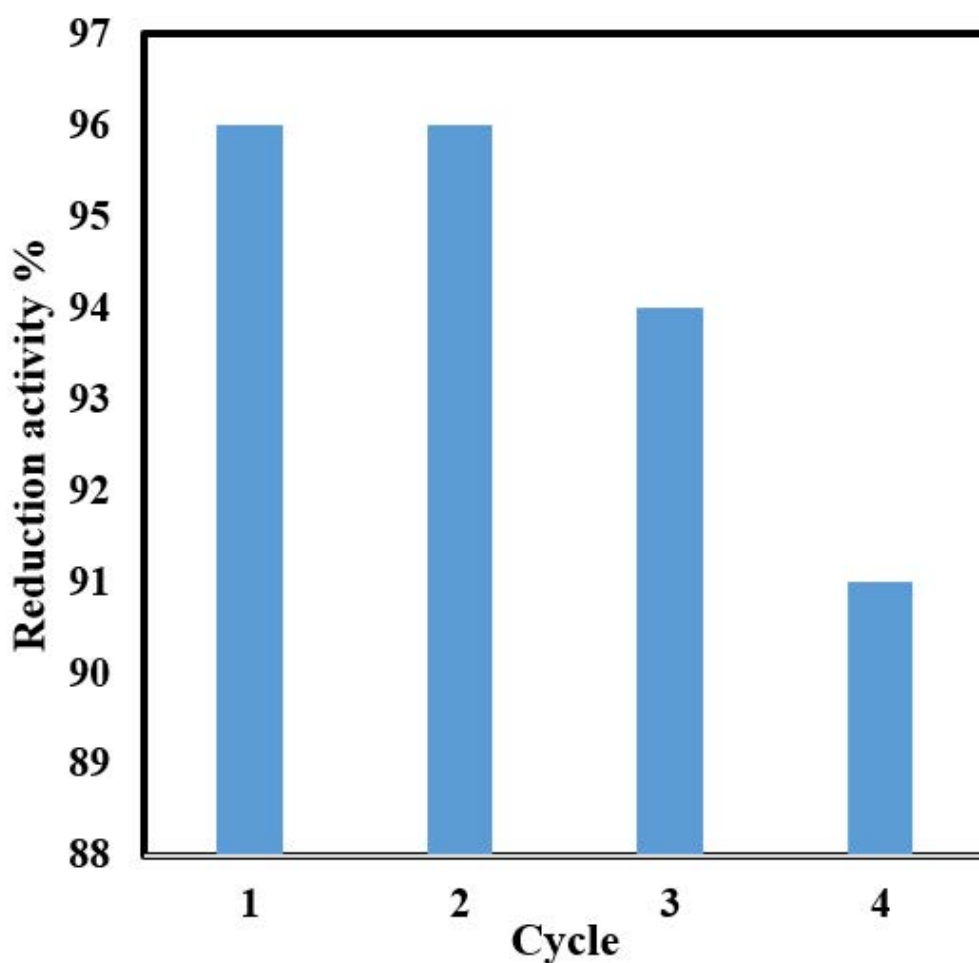| Catalyst | Operating Conditions | Degradation Efficiency | Ref. | Drawback |
|---|---|---|---|---|
| AuNPs | 1.0 mL of 0.015 M $NaBH_4$, 1.7 mL of 0.2 mM 4-nitrophenol, and 0.3 mL of the AuNPs colloidal suspension. | 100% in 8 min. | [18] | Expensive precursors. |
| PdNPs | $1 \times 10^{-4}$ M of 4-NP (1.5 mL) and $5 \times 10^{-2}$ M$NaBH_4$ (1.0 mL, ice cold) 1 mgL$^{-1}$ (0.5 mL) of PdNBs. | 100% in 30 min. | [17] | Complicated synthesis, and flow of nitrogen. |
| Zerovalent iron NPs | 4-NP (50 mgL$^{-1}$) and 1.5% Pd/NZVI catalyst. | 100% in 5 min. | [65] | Use of $NaBH_4$ during synthesis. |
| Chitosan/CuNPs | 100 μL of the colloidal catalyst, $KBH_4$ solution. and 20 μL of $4.66 \times 10^{-2}$ M p-NP. | 100% in 30 min. | [66] | Use of $KBH_4$ during synthesis. |
| $Co_9S_8$ nanotubes | $1.0 \times 10^{-2}$ M (4-nitrophenol), $2.0 \times 10^{-2}$ M ($NaBH_4$) and 10 mg L$^{-1}$ ($Co_9S_8$ nanotubes). | 100% in 8 min. | [26] | Complicated synthesis, |
| MOFs-derived N-doped carbon | | 100% in 10 min. | [12] | Complicated synthesis, |
| Carbon nanotube/Pd NPs | 2 mL of 4-nitrophenol aqueous ($5 \times 10^{-5}$ M) and 1 mL of $NaBH_4$ (0.05 M) and 100 mL of catalyst (0.05 gL$^{-1}$) | 100% in 7 min. | [67] | Complicated synthesis, |
| $MnO_2$/Zeolite | 3 mL of 20 mgL$^{-1}$ pN, P 1 mg of $NaBH_4$, and 10 mg of $MnO_2$/Zeolite. | 96% in 9 min. | This work | Simple synthesis |



**Figure 13.** The efficiency of the catalytic reduction of pNP over Mn2Z. The reduction conditions were: 3 mL of 20 mgL$^{-1}$ pNP solution, 1 mg $NaBH_4$, and 10 mg of the catalyst for 10 min.

## 5. Conclusions

Zeolite-supported MnO$_2$ nanocomposite catalysts were synthesized successfully by utilizing plant extract as a stabilizing and capping agent. The synthesis route followed in this work was very simple, eco-friendly, cost-effective, and utilized very mild conditions. The catalytic efficiency of the nanocomposites was tested through the reduction of p-nitrophenol into p-aminophenol. Results indicated that almost 100% reduction was achieved in less than 30 min. Results of this study showed that a zeolite-supported MnO$_2$ catalyst is very promising for the reduction of organic pollutants. Furthermore, the reusability of the catalyst was tested, and the results showed that 95% of the activity was maintained after four successive cycles, which is very important for commercial application.

**Author Contributions:** Conceptualization, E.D. and A.T.; methodology, E.D. and A.T.; formal analysis, E.D. and A.T.; data curation, E.D., A.T. and M.R.E.-A.; writing—original draft preparation, E.D.; writing—review and editing, E.D., A.T. and M.R.E.-A.; project administration, E.D.; funding acquisition, E.D. All authors have read and agreed to the published version of the manuscript.

**Data Availability Statement:** Data available upon request.

**Conflicts of Interest:** The authors declare no conflict of interest.

## References

1. Kumar, R.; Barakat, M.; Daza, Y.; Woodcock, H.; Kuhn, J. EDTA functionalized silica for removal of Cu (II), Zn (II) and Ni (II) from aqueous solution. *J. Colloid. Interface Sci.* **2013**, *408*, 200–205. [CrossRef]
2. Molina, H.R.; Muñoz, J.S.; Leal, M.D.; Reina, T.; Ivanova, S.; Gallego, M.C.; Odriozola, J. Carbon Supported Gold Nanoparticles for the Catalytic Reduction of 4-Nitrophenol. *Front. Chem.* **2019**, *7*, 1–13. [CrossRef]
3. El-Sheikh, S.; Ismail, A.; Al-Sharab, J. Catalytic reduction of p-nitrophenol over precious metals/highly ordered mesoporous silica. *New J. Chem.* **2013**, *37*, 2399–2407. [CrossRef]
4. Sismanoglu, T.; Pura, S. Adsorption of aqueous nitrophenols on clinoptilolite, Colloids Surfaces A Physicochem. *Eng. Asp.* **2001**, *180*, 1–6. [CrossRef]
5. Urkude, K.; Thakare, S.; Gawande, S. An energy efficient photocatalytic reduction of 4-nitrophenol. *J. Environ. Chem. Eng.* **2014**, *2*, 759–764. [CrossRef]
6. Tabatabaei, S.; Dastmalchi, S.; Mehrizad, A.; Gharbani, P. Enhancement of 4-nitrophenol ozonation in water by nano ZnO catalyst. *Iran. J. Environ. Heal. Sci. Eng.* **2011**, *8*, 363–372.
7. Yahya, A.; Rashid, K.; Ghadhban, M.; Mousa, N.; Majdi, H.; Salih, I.; Alsalhy, Q. Removal of 4-nitrophenol from aqueous solution by using polyphenylsulfone-based blend membranes: Characterization and performance. *Membranes* **2021**, *11*, 171. [CrossRef]
8. Naje, A.; Abbas, S. Electrocoagulation Technology in Wastewater Treatment: A Review of Methods and Applications. *Civ. Environ. Res.* **2013**, *3*, 29–42. Available online: http://www.iiste.org/Journals/index.php/CER/article/view/8115 (accessed on 20 January 2023).
9. Ma, T.; Liang, F.; Chen, R.; Liu, S.; Zhang, H. Synthesis of Au-Pd bimetallic nanoflowers for catalytic reduction of 4-nitrophenol. *Nanomaterials* **2017**, *7*, 239. [CrossRef]
10. Das, N.C.; Das, T.K. Advances on catalytic reduction of 4-nitrophenol by nanostructured materials as benchmark reaction. *Int. Nano Lett.* **2022**, *12*, 223–242. [CrossRef]
11. Lu, H.; Qiao, X.; Wang, W.; Tan, F.; Xiao, Z.; Chen, J. Chitosan stabilised nanozero-valent iron for the catalytic reduction of p-nitrophenol. *Micro Nano Lett.* **2014**, *9*, 446–450. [CrossRef]
12. Wang, Z.; Chen, Q. Metal-free catalytic reduction of 4-nitrophenol by MOFs-derived N-doped carbon. *ChemistrySelect* **2018**, *3*, 1108–1112. [CrossRef]
13. Tian, Y.; Cao, Y.; Pang, F.; Chen, G.; Zhang, X. Ag nanoparticles supported on N-doped graphene hybrids for catalytic reduction of 4-nitrophenol. *RSC Adv.* **2014**, *4*, 43204–43211. [CrossRef]
14. Nekoeinia, M.; Yousefinejad, S.; Hasanpour, F.; Yousefian-Dezaki, M. Highly efficient catalytic degradation of p-nitrophenol by Mn$_3$O$_4$.CuO nanocomposite as a heterogeneous fenton-like catalyst. *J. Exp. Nanosci.* **2020**, *15*, 322–336. [CrossRef]
15. Mehmood, S.; Janjua, N.; Saira, F.; Fenniri, H. AuCu@Pt nanoalloys for catalytic application in reduction of 4-nitrophenol. *J. Spectrosc.* **2016**, *2016*, 6210794. [CrossRef]
16. Kong, X.; Sun, Z.; Chen, M.; Le Chen, C.; Chen, Q. Metal-free catalytic reduction of 4-nitrophenol to 4-aminophenol by N-doped graphene. *Energy Environ. Sci.* **2013**, *6*, 3260–3266. [CrossRef]

17. Kalekar, A.; Sharma, K.; Luwang, M.; Sharma, G. Catalytic activity of bare and porous palladium nanostructures in the reduction of 4-nitrophenol. *RSC Adv.* **2016**, *6*, 11911–11920. [CrossRef]

18. Noël, S.; Bricout, H.; Addad, A.; Sonnendecker, C.; Zimmermann, W.; Monflier, E.; Léger, B. Catalytic reduction of 4-nitrophenol with gold nanoparticles stabilized by large-ring cyclodextrins. *New J. Chem.* **2020**, *44*, 21007–21011. [CrossRef]

19. Lin, C.; Tao, K.; Hua, D.; Ma, Z.; Zhou, S. Size effect of gold nanoparticles in catalytic reduction of p-nitrophenol with $NaBH_4$. *Molecules* **2013**, *18*, 12609–12620. [CrossRef] [PubMed]

20. Yusuf, T.; Ogundare, S.; Pillay, M.; van Zyl, W. Heptanuclear Silver Hydride Clusters as Catalytic Precursors for the Reduction of 4-Nitrophenol. *Molecules* **2022**, *27*, 5223. [CrossRef]

21. Jiang, Z.; Xie, J.; Jiang, D.; Wei, X.; Chen, M. Modifiers-assisted formation of nickel nanoparticles and their catalytic application to p-nitrophenol reduction. *CrystEngComm* **2013**, *15*, 560–569. [CrossRef]

22. Sun, J.; Li, M.; Sun, X.; Wang, L.; Han, P.; Qi, G.; Gao, D.; Zhang, L.; Tao, S. Copper-Based Integral Catalytic Impeller for the Rapid Catalytic Reduction of 4-Nitrophenol. *ACS Omega* **2021**, *6*, 21784–21791. [CrossRef] [PubMed]

23. Kalarivalappil, V.; Divya, C.; Wunderlich, W.; Pillai, S.; Hinder, S.; Nageri, M.; Kumar, V.; Vijayan, B. Pd Loaded $TiO_2$ Nanotubes for the Effective Catalytic Reduction of p-Nitrophenol. *Catal. Lett.* **2016**, *146*, 474–482. [CrossRef]

24. Sahu, K.; Singhal, R.; Mohapatra, S. Morphology Controlled CuO Nanostructures for Efficient Catalytic Reduction of 4-Nitrophenol. *Catal. Lett.* **2020**, *150*, 471–481. [CrossRef]

25. Yazid, H.; Atikah, N.; Rahman, A. Catalytic reduction of p -nitrophenol on Au / $TiO_2$ powder and Au / $TiO_2$ membrane Catalytic Reduction of p -Nitrophenol on Au / $TiO_2$ Powder and Au / $TiO_2$ Membrane. *AIP Conf. Proc.* **2021**, *2332*, 070004.

26. Geng, T.; Ni, Y.; Wang, H.; Zhou, X. $Co_9S_8$ nanotubes: Facile synthesis and application in the catalytic reduction of 4-nitrophenol. *Bull. Mater. Sci.* **2016**, *39*, 1501–1505. [CrossRef]

27. Zhou, L.; Wen, M.; Wu, Q.; Wu, D. Fabrication and catalytic activity of FeNi Ni nanocables for the reduction of p-nitrophenol. *J. Chem. Soc. Dalt. Trans.* **2014**, *43*, 7924–7929. [CrossRef]

28. Cyganowski, P.; Dzimitrowicz, A. Heterogenous nanocomposite catalysts with rhenium nanostructures for the catalytic reduction of 4-nitrophenol. *Sci. Rep.* **2022**, *12*, 6228. [CrossRef]

29. Kästner, C.; Thünemann, A. Catalytic Reduction of 4-Nitrophenol Using Silver Nanoparticles with Adjustable Activity. *Langmuir* **2016**, *32*, 7383–7391. [CrossRef]

30. Shaik, M.; Adil, S.; Kuniyil, M.; Sharif, M.; Alwarthan, A.; Siddiqui, M.; Ali, M.; Tahir, M.; Khan, M. Facile sonochemical preparation of au-$ZrO_2$ nanocatalyst for the catalytic reduction of 4-nitrophenol. *Appl. Sci.* **2020**, *10*, 503. [CrossRef]

31. Punnoose, M.S.; Bijimol, D.; Mathew, B. Microwave assisted green synthesis of gold nanoparticles for catalytic degradation of environmental pollutants, Environ. Nanotechnology. *Monit. Manag.* **2021**, *16*, 100525. [CrossRef]

32. Qi, B.; Wu, C.; Liu, Y.; Liu, J.; Zhang, H. Self-Assembled Magnetic Pt Nanocomposites for the Catalytic Reduction of Nitrophenol. *ACS Appl. Nano Mater.* **2019**, *2*, 4377–4385. [CrossRef]

33. Saira, F.; Saleemi, S.; Razzaq, H.; Qureshi, R. Spectrophotometric analysis of stability of gold nanoparticles during catalytic reduction of 4-nitrophenol. *Turkish J. Chem.* **2021**, *45*, 82–91. [CrossRef] [PubMed]

34. Wu, Z.; Zhang, Y.; Wang, X.; Zou, Z. Ag@$SrTiO_3$ nanocomposite for super photocatalytic degradation of organic dye and catalytic reduction of 4-nitrophenol. *New J. Chem.* **2017**, *41*, 5678–5687. [CrossRef]

35. Madhushree, R.; Resnik, J.; Jaleel, U.C.; Pinheiro, D.; Devi, K.R.S. The catalytic reduction of 4-nitrophenol using $MoS_2$/ZnO nanocomposite. *Appl. Surf. Sci. Adv.* **2022**, *10*, 100265. [CrossRef]

36. Shen, Y.; Sun, Y.; Zhou, L.; Li, Y.; Yeung, E. Synthesis of ultrathin PtPdBi nanowire and its enhanced catalytic activity towards p-nitrophenol reduction. *J. Mater. Chem. A* **2014**, *2*, 2977–2984. [CrossRef]

37. Taha, A.; Aissa, M.B.; Da'na, E. Green synthesis of an activated carbon-supported Ag and ZnO nanocomposite for photocatalytic degradation and its antibacterial activities. *Molecules* **2020**, *25*, 1586. [CrossRef]

38. Ibrahim, A.; Salama, R.; El-Hakam, S.; Khder, A.; Ahmed, A. Synthesis of 12-tungestophosphoric acid supported on Zr/MCM-41 composite with excellent heterogeneous catalyst and promising adsorbent of methylene blue. *Colloids Surfaces A Physicochem. Eng. Asp.* **2021**, *631*, 127753. [CrossRef]

39. Ma, Z.; Qiu, Y.; Huang, Y.; Gao, F.; Hu, P. Chitosan assisted synthesis of 3D graphene@Au nanosheet composites: Catalytic reduction of 4-nitrophenol. *RSC Adv.* **2015**, *5*, 79456–79462. [CrossRef]

40. Kalhor, M.; Samiei, S.; Mirshokraie, S. $MnO_2$@Zeolite-Y Nanoporous: Preparation and Application as a High Efficient Catalyst for Multi-Component Synthesis of 4-Arylidene-Isoxazolidinones. *Silicon* **2021**, *13*, 201–210. [CrossRef]

41. Boroglu, M.S.; Gurkaynak, M.A. Fabrication and characterization of silica modified polyimide-zeolite mixed matrix membranes for gas separation properties. *Polym. Bull.* **2011**, *66*, 463–478. [CrossRef]

42. Bahari, N.A.; Isahak, W.N.R.W. Selective Short Chain Carboxylic Acid Production over Fe:Zeolite Nanoparticles from $CO_2$ Hydrogenation Reaction. *IOP Conf. Ser. Mater. Sci. Eng.* **2020**, *778*, 012070. [CrossRef]

43. Endang, P.S.; Rahadian, A.R.; Ulva, T.I.M.; Alvin, R.W.; Rendy, M.I.; Nurul, W. The $MnO_2$/zeolite nay catalyzed oxidation of co emission in catalytic converter system. *Mater. Sci. Forum.* **2019**, *964*, 199–208. [CrossRef]

44. Prasetyo, T.A.B.; Soegijono, B. Characterization of sonicated natural zeolite/ferric chloride hexahydrate by infrared spectroscopy. *J. Phys. Conf. Ser.* **2018**, *985*, 012022. [CrossRef]

45. Da'na, E.; Taha, A.; Afkar, E. Green synthesis of iron nanoparticles by Acacia nilotica pods extract and its catalytic, adsorption, and antibacterial activities. *Appl. Sci.* **2018**, *8*, 1922. [CrossRef]

46. Taha, A.; Da'Na, E.; Hessien, M. Evaluation of catalytic and adsorption activity of iron nanoparticles greenly prepared under different conditions: Box–Behnken design. *Mol. Simul.* **2020**, *48*, 8–18. [CrossRef]

47. Da'na, E.; Taha, A.; Hessien, M. Application of ZnO–NiO greenly synthesized nanocomposite adsorbent on the elimination of organic dye from aqueous solutions: Kinetics and equilibrium. *Ceram. Int.* **2021**, *47*, 4531–4542. [CrossRef]

48. Hessien, M.; Da'na, E.; Taha, A. Phytoextract assisted hydrothermal synthesis of ZnO–NiO nanocomposites using neem leaves extract. *Ceram. Int.* **2021**, *47*, 811–816. [CrossRef]

49. Taha, A.; Da'Na, E. Phyto-Assisted Assembly of Metal Nanoparticles in Chitosan Matrix Using S. argel Leaf Extract and Its Application for Catalytic Oxidation of Benzyl Alcohol. *Polymers* **2022**, *14*, 766. [CrossRef]

50. Hessien, M.; Taha, A.; Da'na, E. Acacia nilotica Pods' Extract Assisted-Hydrothermal Synthesis and Characterization of ZnO-CuO Nanocomposites. *Materials* **2022**, *15*, 2291. [CrossRef]

51. Da'na, E.; Taha, A.; Hassanin, H. Green fabrication of iron nanoparticles decorated with amine functionality for the remediation of lead ions from aqueous solutions. *Surf. Interfaces* **2022**, *30*, 101909. [CrossRef]

52. Triveni, A.; Kumar, M.S.; Shivannavar, C.; Gaddad, S. Antibacterial and antibiofilm activities of crude extracts of Lawsonia inermis against methicillin-resistant Staphylococcus aureus. *Asian J. Pharm. Clin. Res.* **2016**, *9*, 263–265. [CrossRef]

53. Society, S.; Sabra, S.; Al-masoudi, L.; El-, H.; Hasan, M.; Al-gehani, S.; Abu-harbah, A. The Importance of the Chemical Composition of Henna Tree Leaves (Lawsonia inermis) and its Ability to Eliminate Tinea pedis, with Reference to the Extent of Usage and Storage in the Saudi Society, Taif, KSA. *Semant. Sch.* **2015**, *10*, 23–29. [CrossRef]

54. Dawadi, S.; Gupta, A.; Khatri, M.; Budhathoki, B.; Lamichhane, G.; Parajuli, N. Manganese dioxide nanoparticles: Synthesis, application and challenges. *Bull. Mater. Sci.* **2020**, *43*, 277. [CrossRef]

55. Tran, N.; Duong, N.; Le, N. Synthesis and Characterization of Magnetic $Fe_3O_4$/Zeolite NaA Nanocomposite for the Adsorption Removal of Methylene Blue Potential in Wastewater Treatment. *J. Chem.* **2021**, *2021*, 6678588. [CrossRef]

56. Souri, M.; Hoseinpour, V.; Shakeri, A.; Ghaemi, N. Optimisation of green synthesis of MnO nanoparticles via utilising response surface methodology. *IET Nanobiotechnology* **2018**, *12*, 822–827. [CrossRef] [PubMed]

57. Sannasi, V.; Subbian, K. Influence of Moringa oleifera gum on two polymorphs synthesis of $MnO_2$ and evaluation of the pseudo-capacitance activity. *J. Mater. Sci. Mater. Electron.* **2020**, *31*, 17120–17132. [CrossRef]

58. Lu, H.; Zhang, X.; Khan, S.; Li, W.; Wan, L. Biogenic Synthesis of $MnO_2$ Nanoparticles With Leaf Extract of Viola betonicifolia for Enhanced Antioxidant, Antimicrobial, Cytotoxic, and Biocompatible Applications. *Front. Microbiol.* **2021**, *12*, 761084. [CrossRef] [PubMed]

59. Ramakrishna, C.; Saini, B.; Racharla, K.; Gujarathi, S.; Sridara, C.; Gupta, A.; Thakkallapalli, G.; Rao, P. Rapid and complete degradation of sulfur mustard adsorbed on M/zeolite-13X supported (M = 5 wt% Mn, Fe, Co) metal oxide catalysts with ozone. *RSC Adv.* **2016**, *6*, 90720–90731. [CrossRef]

60. Su, F.; Lu, C. $CO_2$ capture from gas stream by zeolite 13X using a dual-column temperature/vacuum swing adsorption. *Energy Environ. Sci.* **2012**, *5*, 9021–9027. [CrossRef]

61. Xu, J.; Xiao, X.; Stepanov, A.; Ren, F.; Wu, W.; Cai, G.; Zhang, S.; Dai, Z.; Mei, F.; Jiang, C. Efficiency enhancements in Ag nanoparticles-$SiO_2$-$TiO_2$ sandwiched structure via plasmonic effect-enhanced light capturing. *Nanoscale Res. Lett.* **2013**, *8*, 73. [CrossRef] [PubMed]

62. Das, T.K.; Ganguly, S.; Remanan, S.; Ghosh, S.; Das, N.C. Mussel-inspired Ag/poly(norepinephrine)/$MnO_2$ heterogeneous nanocatalyst for efficient reduction of 4-nitrophenol and 4-nitroaniline: An alternative approach. *Res. Chem. Intermed.* **2020**, *46*, 3629–3650. [CrossRef]

63. Zhang, P.; Sui, Y.; Xiao, G.; Wang, Y.; Wang, C.; Liu, B.; Zou, G.; Zou, B. Facile fabrication of faceted copper nanocrystals with high catalytic activity for p-nitrophenol reduction. *J. Mater. Chem. A* **2013**, *1*, 1632–1638. [CrossRef]

64. Dai, Y.; Ren, T.; Wang, Y.; Zhang, X. Polyion complex micelles to stabilize gold nanoparticles for catalytic reduction of 4-nitrophenol. *Gold Bull.* **2018**, *51*, 21–26. [CrossRef]

65. Tokazhanov, G.; Han, S.; Lee, W. Enhanced catalytic reduction of p-nitrophenol by nano zerovalent iron-supported metal catalysts. *Catal. Commun.* **2021**, *158*, 106337. [CrossRef]

66. Tan, W.L.; Abu Bakar, N.H.H.; Abu Bakar, M. Catalytic reduction of p-nitrophenol using chitosan stabilized copper nanoparticles. *Catal. Lett.* **2015**, *145*, 1626–1633. [CrossRef]

67. Gu, X.; Qi, W.; Xu, X.; Sun, Z.; Zhang, L.; Liu, W.; Pan, X.; Su, D. Covalently functionalized carbon nanotube supported Pd nanoparticles for catalytic reduction of 4-nitrophenol. *Nanoscale* **2014**, *6*, 6609–6616. [CrossRef]